Ultrabroad Terahertz Spectrum Generation from an Air-Based Filament Plasma

V. A. Andreeva,[1] O. G. Kosareva,[1,2,*] N. A. Panov,[2] D. E. Shipilo,[1] P. M. Solyankin,[1] M. N. Esaulkov,[3] P. González de Alaiza Martínez,[4] A. P. Shkurinov,[1,2] V. A. Makarov,[1,2] L. Bergé,[4] and S. L. Chin[5]
[1]Faculty of Physics, Lomonosov Moscow State University, 119991 Leninskie gori 1/2, Moscow, Russia
[2]International Laser Center, Lomonosov Moscow State University, 119991 Leninskie gori 1/62, Moscow, Russia
[3]Institute on Laser and Information Technologies of the Russian Academy of Sciences (ILIT RAS), 140700 Shatura, Russia
[4]CEA-DAM, DIF, 91297 Arpajon, France
[5]Département de Physique, de Génie Physique et d'Optique, Centre d'Optique, Photonique et Laser (COPL), Université Laval, Québec, QC G1V 0A6, Canada
(Received 11 September 2015; published 11 February 2016)

We have solved the long-standing problem of the mechanism of terahertz (THz) generation by a two-color filament in air and found that both neutrals and plasma contribute to the radiation. We reveal that the contribution from neutrals by four-wave mixing is much weaker and higher in frequency than the distinctive plasma lower-frequency contribution. The former is in the forward direction while the latter is in a cone and reveals an abrupt down-shift to the plasma frequency. Ring-shaped spatial distributions of the THz radiation are shown to be of universal nature and they occur in both collimated and focusing propagation geometries. Experimental measurements of the frequency-angular spectrum generated by 130-fs laser pulses agree with numerical simulations based on a unidirectional pulse propagation model.

DOI: 10.1103/PhysRevLett.116.063902

Laser filamentation [1–6] is actively studied because of both traditional applications, e.g., a wideband atmospheric lamp [7], and newly emerging filament-based spectroscopy techniques [8]. Filament plasmas can promote continuous spectral bandwidths from 0.1 [9] to 20–100 THz depending on the pulse duration [10,11]. Coherent terahertz (THz) radiation can then be delivered through the filamentation process to a desired remote position in the atmosphere, thereby avoiding its absorption by water vapor [12,13]. Experiments on the spatial profile of THz radiation from laser plasmas demonstrated that this radiation propagates inside a cone and forms a ring in the far field [11,14–18].

Three major physical reasons of THz generation in a two-color air filament are often proposed in the literature, namely, rectification by four-wave mixing (Kerr or bound electron response) [19,20], plasma currents induced by tunneling ionization [21–24], as well as transverse and longitudinal plasma wave excitations [25–28]. In this work we suggest the generalized numerical approach allowing one to describe the observed phenomena on a unified basis including optical nonlinearities and plasma effects as well. Through this approach and our experiment we have solved the long-standing problem of the mechanism of THz generation in a two-color filament, namely, both neutrals and plasma contribute to the radiation, not just one of them. We reveal that the contribution from neutrals by four-wave mixing is much weaker and it occurs at higher frequencies than the distinctive plasma lower-frequency contribution. The former process emits in the forward direction while the latter lies in a cone. The neutral contribution arises mainly from the front part of the self-focusing laser pulse, which always sees the neutral gas as it propagates. At later times, when plasma defocusing occurs, free-electron photocurrents overwhelm the contribution from neutral molecules and emit conically [13–18]. Numerical simulations confirm the universality of these ring-shaped THz distributions due to the conical emission. At the intensities involved, plasma wakefield effects are shown to be limited.

In our experiment the 800-nm beam supplied by a Ti:sapphire regenerative amplifier (Spectra Physics Spitfire Pro, 130 fs, <1.5 mJ, 800 nm, 1 kHz) is focused with a $f = 15$ cm plano-convex lens into ambient air [Fig. 1(a)]. A 0.1-mm thick beta barium borate (β-BBO) crystal (I type) adjusted to reach the maximum THz yield is used for generating the second harmonic. A 1.5-cm laser spark formed near the geometrical focus locates the emitted THz radiation, which is collimated using an off-axis parabolic mirror (51.6 mm in diameter, 150-mm effective focal length). A 0.35-mm thick silicon wafer filters the radiated field. To investigate the frequency-angular terahertz spectrum we couple a Michelson interferometer to a liquid helium-cooled silicon bolometer $\mathrm{LN}-6/\mathrm{C}$ (Infrared Laboratories), used as a detector of the THz radiation. A 3.5-mm thick high-resistive silicon beam splitter (Tydex HRFZ-Si) (54% transmittance) with 50-mm aperture is employed for separation and recombination of the two arms of the interferometer ending with flat metallic mirrors, one of which is placed on a motorized translation stage. After recombination, the THz beam is refocused with an off-axis parabolic mirror into the aperture of the bolometer with filters transparent in the THz region (e.g., <24 THz). Typical interferograms have 500–800 points with 2.5-μm increment ensuring spectral resolution up to 75 GHz. The reconstruction of the THz spectrum is done using the

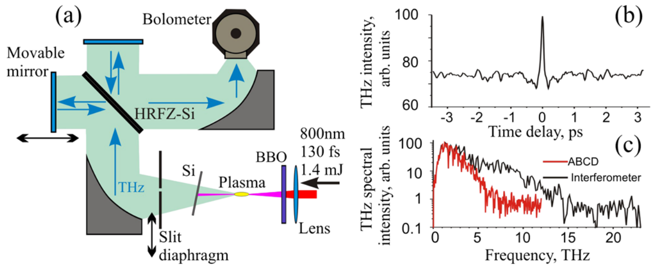

FIG. 1. (a) Experimental setup. Note the slit moved across the THz transverse profile to scan the conical emission. (b) Typical interferogram and (c) THz spectrum (black curve), compared to that obtained with the ABCD technique (red curve).

Fourier transform of the THz signal autocorrelation function.

THz spectra recorded from 50 averaged interferograms have been obtained using 1.4-mJ, 130-fs two-color pulses with ~10% fraction of second harmonic in amplitude. The resulting THz field is displayed in Fig. 1(b), while Fig. 1(c) details the spectrum plotted from our interferograms (black curve). The spectrum reaches noise level at 15 THz while the signal measured in similar conditions using the air-biased coherent detection (ABCD) method [10,14] reaches noise level at 6–7 THz [cf. black and red curves of Fig. 1(c)]. Thus, our autocorrelation experimental technique is adequate for the study of broadband THz spectra.

The measured spectra in the range 0–30 THz are integrated over a 12-mm transverse aperture [Fig. 2(a), black dots]. The red curve plots numerical spectra computed from a unidirectional pulse propagation equation (UPPE) for comparable laser inputs (see below). The experimentally measured THz spectrum is in good agreement with the simulated one. A maximum at around 0.5–1 THz in the experimentally obtained spectrum is due to the photocurrent induced by the plasma, creating a peak around the electron plasma frequency, $\nu_{pe} = \omega_{pe}/2\pi = (e^2 N_e/\pi m)^{1/2} \approx 0.75$ THz, where $N_e \approx 7\times 10^{15}$ cm^{-3} is the typical free-electron density for filaments, e and m are the electron charge and mass. The spectral amplitudes at higher frequencies $\nu > 12.5$ THz are more attenuated in the experiment because of absorption by the HRFZ-Si beam splitter and filters used in our setup. In addition, we performed measurements of frequency-angular spectra of the THz radiation by moving a 1.5-mm slit across the diverging THz beam before collimation [Fig. 1(a)]. The angular distribution of THz radiation exhibits a maximum in the emission direction at 4–6 deg relative to the beam propagation axis [white dashed lines in Figs. 2(b) and 2(c)]. The off-axis maximum in the frequency-angular distribution corresponds to a ring in the far zone. In both the experiment and the simulations 15% of the THz energy in the range 0.5–13 THz propagates forwardly (on axis) and 85% in the ring. The overall THz radiation energy in the range 0–30 THz is 9 nJ.

Because THz emissions also proceed from plasma wave oscillations, Figs. 2(d) and 2(e) detail the low-frequency spectra of field components $\vec{\tilde{E}}$ radiated in the transverse and longitudinal directions as computed from the nonpropagating plasma fluid model combining derivations from Refs. [25–28]:

$$\left(\frac{\partial^2}{\partial t^2} + \nu_c \frac{\partial}{\partial t} + \omega_{pe}^2\right)\vec{\tilde{E}} = -4\pi\left(\vec{\Pi} + \frac{\partial \vec{J}_e}{\partial t} + \frac{\partial^2 \vec{P}}{\partial t^2}\right). \quad (1)$$

Here $\vec{J}_e$ and $\vec{P}$ denote the electron current density and Kerr polarization computed with the given nonpropagating laser field, $\nu_c \approx 5$ ps^{-1} is the electron-neutral collision frequency [27]. In the transverse plane of the 800-nm pulse polarization direction, the radiated electromagnetic field is due to the photocurrents through the derivative $\partial \vec{J}_e/\partial t$ [21]. Longitudinal low-frequency currents can also originate from the $\vec{\Pi}$ source term derived in Refs. [25–28], which gathers radiation pressure and ponderomotive effects. Figures 2(d) and 2(e) clearly confirm that, for the laser and material parameters used in the experiment, (i) the transverse field component prevails over the longitudinal one at $\nu > 1$ THz and (ii) a plasma wave emerges over time scales longer than the laser pulse duration, which explains the spectral peak reached at ν_{pe}. Beyond the plasma frequency the spectrum rapidly falls down like $1/\nu^2$, faster than in the experiment [cf. Fig. 2(d), gray curve, and Fig. 2(a), black dots]. The Kerr contribution increases the spectral amplitude at frequencies $\nu > \nu_{pe}$ [$\vec{P} \neq \vec{0}$, Fig. 2(d), black curve]. Thus, the spectral wing spreading up to

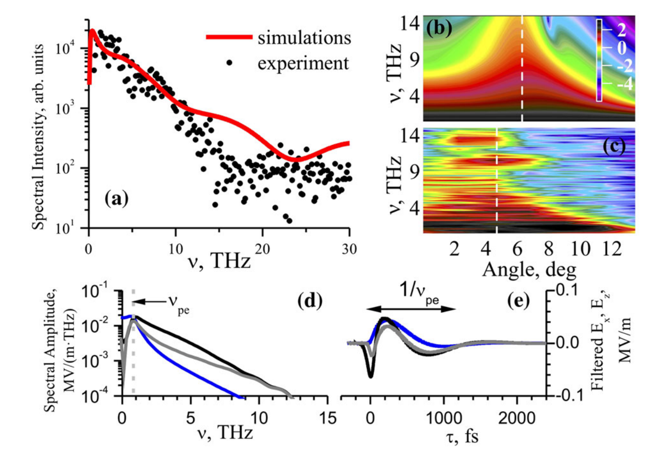

FIG. 2. (a) Experimental (black dots) and simulated (red solid line) THz spectra from a two-color pulse (800 nm: 1.4 mJ, 150 fs; 400 nm: 10 μJ, 220 fs) focused in air ($f = 15$ cm). (b),(c) Frequency-angular distributions: (b) simulation and (c) experiment in logarithmic color scale. Dashed vertical lines show the directions of maximum THz signals. (d) THz spectra peaked at $\nu = \nu_{pe}$ (gray dashed line) and (e) electromagnetic fields computed from the nonpropagating plasma fluid model Eq. (1). The black (gray) curves show the transverse field triggered by photoionization with (without) the Kerr nonlinearity; the blue curves refer to longitudinal plasma wakefields.

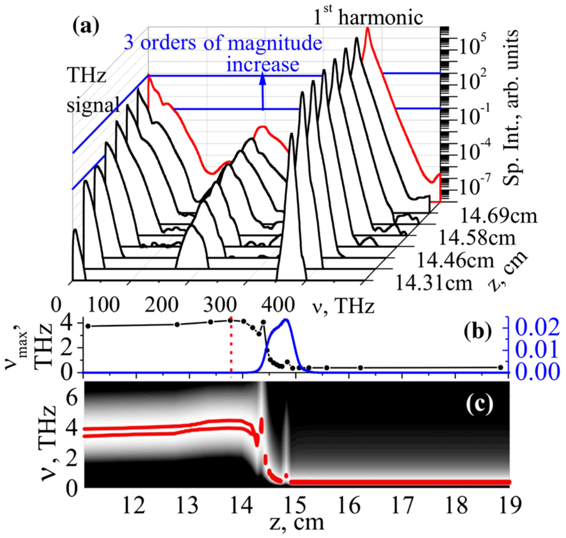

FIG. 3. (a) Simulated frequency spectra along z in the two-color filament. (b) Maximum of the THz spectrum (black circles joined by black line) and peak plasma density (blue line) as function of the propagation distance. Vertical dashed line indicates the position of the maximum THz signal emitted by neutrals. (c) Down-shift of the THz spectral maximum from ∼4 to ∼0.5 THz as indicated by the red contour (99% of the maximum spectral intensity).

30 THz in Fig. 2(a) can be attributed to the nonlinearity of bound electrons.

In light of the previous properties, propagating THz pulses can properly be described by UPPE [29,13]. Advances of the present numerical method are in the simultaneous consideration of a rather broad beam size (3 mm), large nonparaxial radiation divergence (up to 45°), and frequency resolution of 50 GHz in accordance with our experimental setup. We assumed axially symmetric propagation pertinent to the single filament regime of our experiment and implemented the discrete Hankel transform algorithm [30] optimized to ensure correct direct-inverse repetitive field transformations from the radial to angular domains. The field $E(r,\tau,z)$ is linearly polarized, r (z) is the transverse (longitudinal) coordinate, and τ is the time in the moving reference frame. The forwardly propagating Fourier component $\hat{E}(k_r,\omega,z)$ of the field $E(r,\tau,z)$ is given by

$$\left(\frac{\partial}{\partial z}-ik_z\right)\hat{E}(k_r,\omega,z)=-\frac{2\pi\omega}{c^2k_z}[\hat{J}(k_r,\omega,z)-i\omega\hat{P}(k_r,\omega,z)], \tag{2}$$

where $k_z=\sqrt{\omega^2n^2(\omega)/c^2-k_r^2}$ is the longitudinal wave vector, P is the third-order (Kerr) polarization, $n(\omega)$ is the refractive index of air, and c is the speed of light. Current coefficient parameters for air can be found in Ref. [31]. The current J contains the free-electron current J_e and the absorption current J_{abs} related to losses through photo-ionization according to the equations

$$\frac{\partial J_e(\tau)}{\partial\tau}=\frac{e^2}{m}N_e(\tau)E(\tau)-\nu_cJ_e(\tau),$$
$$J_{abs}(\tau)=\frac{U_i}{E(\tau)}\frac{\partial N_e(\tau)}{\partial\tau}. \tag{3}$$

Here U_i is the ionization potential of O_2 or N_2 and N_e is the free-electron density governed by $\partial N_e(\tau)/\partial\tau=W(E(\tau))[N_a-N_e(\tau)]$. $W(E)$ is the single-electron photo-ionization rate given by the Perelomov-Popov-Terent'ev's theory, N_a is the density of neutrals.

The input two-color field,

$$E(r,\tau,z=0)=\exp\left(-\frac{r^2}{2a_0^2}\right)$$
$$\times\left[E_0\exp\left(-\frac{\tau^2}{2\tau_0^2}\right)\cos(\omega_0\tau)+E_1\exp\left(-\frac{\tau^2}{2\tau_1^2}\right)\cos(2\omega_0\tau)\right], \tag{4}$$

contains the fundamental frequency $\nu_0=\omega_0/2\pi=375$ THz at 800 nm and its second harmonic at 750 THz. Geometrical focusing is described by multiplying Eq. (4) by the phase factor $\exp[(i\omega r^2)/(2cf)]$ in the frequency domain, where f is the focal length of the lens.

We first simulate the filamentation and THz spectrum evolution in the experimental conditions involving 800- and 400-nm pulses of 1.4 mJ, 150 fs, and 10 μJ, 220 fs, respectively. The input beam diameter is $2a_0=3$ mm. The length of the plasma channel near focus with $f=15$ cm is ∼1.5 cm. The temporal walk-off between the fundamental and the second harmonic is negligible within 20 cm of the optical path.

The low-frequency part of the filament spectrum is integrated over the whole 12-mm transverse aperture as done in the experiments. As evidenced by Fig. 3(a), our numerical simulations provide new insights into the filament-driven THz spectral dynamics. Close to the early self-focusing Kerr stage ($z\le 14$ cm) where there are almost no free electrons, the nonlinear polarization of neutrals mainly contributes to the emitted THz spectrum. The THz signal from the neutrals reaches a maximum at $z\approx 13.8$ cm [vertical line in Fig. 3(b)] and at a comparatively high frequency of ∼4 THz. We checked that this signal was quantitatively reproduced by the simple four-wave mixing model [19,20].

From there on, a first generation of plasma immediately overwhelms the higher-frequency THz signal from neutral air molecules. As plasma quickly builds up, the THz spectrum changes dramatically with an abrupt down-shift around 0.5–1 THz corresponding to the plasma frequency [Figs. 3(b) and 3(c)]. Starting from $z\ge 15$ cm the down-shifted spectrum corresponds to that typically observed in our experiment [Fig. 2(a)]. The intensity in this down-shifted spectral maximum is about 3 orders of magnitude larger than in the initial Kerr-induced THz emission at $z<14.5$ cm [see blue arrow in Fig. 3(a)]. Domination of the photocurrent mechanism was explicitly shown in

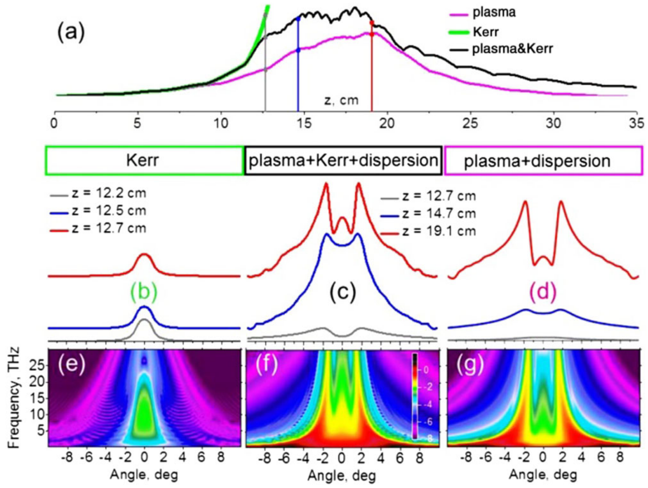

FIG. 4. Simulated conically divergent and on-axis THz emission from the two-color filament. The focal length is $f = 20$ cm, the pump pulse energy is 3.2 mJ and its duration is 54 fs. (a) Filament peak intensity. (b)–(d) THz angular distribution integrated over 0.05–30 THz at indicated distances and propagation media. (e)–(g) Frequency-angular spectra.

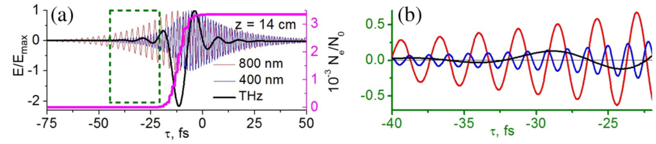

FIG. 5. ω_0 (red) and $2\omega_0$ (blue) optical components, THz field (black), and plasma density (magenta curves) in the complete configuration [as in Figs. 4(c) and 4(f)]. The fields at ω_0, $2\omega_0$, and THz frequency are normalized to their corresponding maximum values $E_{\max}$. (a) Overall pulse and the green frame detailing in (b) the $\omega - 2\omega$ phase matching in the front pulse region.

Ref. [23] by recording the THz yield as a function of the two-color phase difference.

The contribution from the four-wave mixing due to the Kerr nonlinearity can be seen clearly in the developed filament, since it is separated by a small dip at approximately 25 THz starting from $z \approx 14.58$ cm and further in Fig. 3(a). The spectral amplitude at $\omega/2\pi = \nu \geq 25$ THz is almost 3 orders of magnitude less than the peak at $\nu \approx 0.75$ THz, rendering the Kerr contribution masked by the much stronger plasma contribution.

To reveal the physical mechanisms responsible for the on-axis and conical propagation of THz radiation, we now simulate a purely Kerr medium and terminate the simulation as soon as the ionization threshold is reached [see green line interrupted at $z \approx 12.5$ cm in Fig. 4(a)]. The THz spectra remain confined in the forward direction [Fig. 4(e)]. Thus, starting from the onset of filamentation, the on-axis THz source is formed, which moves with the pulse front in the neutral medium and irradiates in the forward direction at each z point along the filament. In contrast, conical emission occurs as plasma defocusing does compete with the Kerr effect [Fig. 4(f)]. The spectral intensity in the ring (red curves) is 2 orders of magnitude larger than at the center (green curves) [Fig. 4(f)]. When there is no Kerr nonlinearity and the plasma only contributes to the spectrum, terahertz conical emission takes place very similarly to the complete configuration [Fig. 4(g)]. Hence, photocurrents produced by plasma generation are the major source of THz radiation [cf. Figs. 4(e) and 4(g)]. The influence of the Kerr response manifests by the enhancement of the forwardly directed THz radiation ["green" maximum in Fig. 4(f)], experimentally observed in Refs. [32–34]. The spatial distribution of THz radiation integrated over the 0.05–30-THz range shows an increase in the on-axis THz yield when both free- and bound electron responses are included [cf. Fig. 4(c) and Fig. 4(d)]. The ω_0, $2\omega_0$, and THz radiation extracted by filtering the overall light field exhibit the characteristic phase shift values 0 or π of Kerr-induced THz signals in the pulse front region $-32 < \tau < -20$ fs [19] [Figs. 5(a) and 5(b)]. This confirms that THz radiation born in the front before the plasma rises (at $\tau \approx -20$ fs) is mainly due to four-wave mixing. During our experimental campaign we were able to identify the Kerr-induced broadband THz spectra by using an ABCD detection scheme [10,14] for pump pulse energies of 30–60 μJ, which are below the photoionization threshold (100 μJ) in our focusing geometry.

The results of our self-consistent simulations agree with the interference models [11,16–18], which introduce $\omega - 2\omega$ phase mismatch and plasma dispersion phenomenologically as key mechanisms responsible for pushing the THz emission off axis and leading to ring formation in the far field.

In order to show the universality of the THz conical emission, we finally simulate the propagation of collimated beams and plot their overall frequency-angular spectrum in Fig. 6. The plasma channel length is $\sim$50 cm. The conical emission occupies all the low-frequency region, with an on-axis radiation being less than the conical emission propagating at $\sim 2°$ from axis [see bottom of Fig. 6(a)]. Filtering the transverse distribution at 10, 50, and 100 THz shows the decrease in the field divergence with increasing frequency [cf. ring radius in Figs. 6(b)–6(d)], experimentally reported in Refs. [11,15]. As we have shown in Fig. 3(a), the higher frequencies of the THz and far infrared range are first produced by the Kerr nonlinearity of neutrals from the front

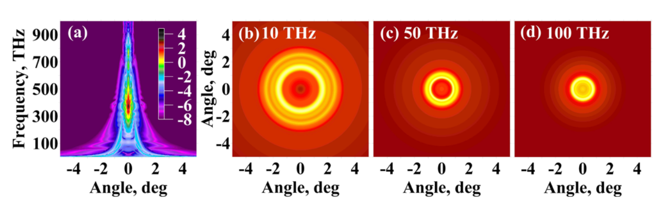

FIG. 6. (a) Simulated frequency-angular spectra in the two-color filament of collimated 800- and 400-nm beams with 54 fs pulse duration, 3.2 mJ and 10-μJ energy, respectively (spectral intensity is in logarithmic color scale). (b–d) Simulated angular distributions for the three selected frequencies of (a).

pulse and they increase the overall forward THz emission. In addition, the natural diffraction is smaller for the higher frequencies. Therefore, at 10 THz we have a ring with 1.8° half-cone angle, at 50 THz the half-cone angle decreases to 1°, and at 100 THz we observe on-axis propagation [Figs. 6(b)–6(d)].

In conclusion, by analyzing the characteristics of THz radiation we have solved the long-standing problem of the mechanism of THz generation in a two-color air filament and demonstrated that both neutrals and plasma contribute to the THz yield. At the onset of filamentation the polarizability of the bound electrons forms an on-axis THz source, which is much weaker than the distinctive free-electron photocurrent THz source. Terahertz radiation from the photocurrent source propagates in a cone.

We displayed evidence of an abrupt down-shift of the spectral peak in the THz spectrum from higher-frequency Kerr contribution toward the electron plasma frequency accompanied by more than 2 orders of magnitude increase in the spectral intensity when photoionization takes place. Ring-shaped spatial distributions of the THz radiation are shown to be of universal nature and they occur in both collimated and focusing propagation geometries. Simulated THz conical distributions and THz spectra agree with the experimental data.

We thank Professor Academician Leonid V. Keldysh, Professor Xi-Cheng Zhang, Professor André Mysyrowicz, and Professor Mikhail V. Fedorov for fruitful discussions and constructive advice. This work is supported by Russian Fund for Basic Research (Grants No. 15-32-20966, No. 15-32-20961, No. 14-22-02021, No. 15-02-99630, No. 14-02-00979), RF President Grant for Leading Scientific Schools (Grant No. NSh-9695.2016.2), Dynasty Foundation, Commissariat à l'Énergie Atomique et aux Énergies Alternatives–France, and Canada Research Chairs. We acknowledge PRACE for awarding us access to the supercomputer CURIE at GENCI@CEA, France.

*kosareva@physics.msu.ru

[1] A. Braun, G. Korn, X. Liu, D. Du, J. Squier, and G. Mourou, Opt. Lett. **20**, 73 (1995).
[2] S. L. Chin, S. A. Hosseini, W. Liu, Q. Luo, F. Théberge, N. Aközbek, A. Becker, V. P. Kandidov, O. G. Kosareva, and H. Schroeder, Can. J. Phys. **83**, 863 (2005).
[3] A. Couairon and A. Mysyrowicz, Phys. Rep. **441**, 47 (2007).
[4] L. Bergé, S. Skupin, R. Nuter, J. Kasparian, and J. Wolf, Rep. Prog. Phys. **70**, 1633 (2007).
[5] V. P. Kandidov, S. A. Shlenov, and O. G. Kosareva, Quantum Electron. **39**, 205 (2009).
[6] S. L. Chin *et al.*, Laser Phys. **22**, 1 (2012).
[7] L. Wöste, C. Wedekind, H. Wille, P. Rairoux, B. Stein, S. Nikolov, Ch. Werner, S. Niedermeier, F. Ronneberger, H. Schillinger, and R. Sauerbrey, Laser und Optoelektronik **29**, 51 (1997).
[8] J. H. Odhner and R. J. Levis, Annu. Rev. Phys. Chem. **65**, 605 (2014).
[9] A. Houard, Y. Liu, B. Prade, V. T. Tikhonchuk, and A. Mysyrowicz, Phys. Rev. Lett. **100**, 255006 (2008).
[10] N. Karpowicz, X. Lu, and X.-C. Zhang, J. Mod. Opt. **56**, 1137 (2009).
[11] V. Blank, M. D. Thomson, and H. G. Roskos, New J. Phys. **15**, 075023 (2013).
[12] X. Xie, J. Dai, and X. C. Zhang, Phys. Rev. Lett. **96**, 075005 (2006).
[13] L. Bergé, S. Skupin, C. Köhler, I. Babushkin, and J. Herrmann, Phys. Rev. Lett. **110**, 073901 (2013).
[14] A. V. Borodin, M. N. Esaulkov, I. I. Kuritsyn, I. A. Kotelnikov, and A. P. Shkurinov, J. Opt. Soc. Am. B **29**, 1911 (2012).
[15] P. Klarskov, A. C. Strikwerda, K. Iwaszczuk, and P. U. Jepsen, New J. Phys. **15**, 075012 (2013).
[16] T. I. Oh, Y. S. You, N. Jhajj, E. W. Rosenthal, H. M. Milchberg, and K. Y. Kim, New J. Phys. **15**, 075002 (2013).
[17] Y. S. You, T. I. Oh, and K. Y. Kim, Phys. Rev. Lett. **109**, 183902 (2012).
[18] A. Gorodetsky, A. D. Koulouklidis, M. Massaouti, and S. Tzortzakis, Phys. Rev. A **89**, 033838 (2014).
[19] D. J. Cook and R. M. Hochstrasser, Opt. Lett. **25**, 1210 (2000).
[20] A. V. Borodin, N. A. Panov, O. G. Kosareva, V. A. Andreeva, M. N. Esaulkov, V. A. Makarov, A. P. Shkurinov, S. L. Chin, and X.-C. Zhang, Opt. Lett. **38**, 1906 (2013).
[21] K. Y. Kim, A. J. Taylor, J. H. Glownia, and G. Rodriguez, Nat. Photonics **2**, 605 (2008).
[22] I. Babushkin, S. Skupin, A. Husakou, C. Köhler, E. Cabrera-Granado, L. Bergé, and J. Herrmann, New J. Phys. **13**, 123029 (2011).
[23] M. Li, W. Li, Y. Shi, P. Lu, H. Pan, and H. Zeng, Appl. Phys. Lett. **101**, 161104 (2012).
[24] J. Wu, Y. Tong, M. Li, H. Pan, and H. Zeng, Phys. Rev. A **82**, 053416 (2010).
[25] A. Debayle, L. Gremillet, L. Bergé, and Ch. Köhler, Opt. Express **22**, 13691 (2014).
[26] A. V. Balakin, A. V. Borodin, I. A. Kotelnikov, and A. P. Shkurinov, J. Opt. Soc. Am. B **27**, 16 (2010).
[27] P. Sprangle, J. R. Peñano, B. Hafizi, and C. A. Kapetanakos, Phys. Rev. E **69**, 066415 (2004).
[28] C. D'Amico, A. Houard, S. Akturk, Y. Liu, J. Le Bloas, M. Franco, B. Prade, A. Couairon, V. T. Tikhonchuk, and A. Mysyrowicz, New J. Phys. **10**, 013015 (2008).
[29] M. Kolesik and J. V. Moloney, Phys. Rev. E **70**, 036604 (2004).
[30] H. F. Johnston, Comput. Phys. Commun. **43**, 181 (1987).
[31] *Handbook of Chemistry and Physics* (CRC Press, Boca Raton, FL, 1985).
[32] Y. Chen, C. Marceau, W. Liu, Z.-D. Sun, Y. Zhang, F. Théberge, M. Châteauneuf, J. Dubois, and S. L. Chin, Appl. Phys. Lett. **93**, 231116 (2008).
[33] Y. Chen, C. Marceau, S. Génier, F. Théberge, M. Châteauneuf, J. Dubois, and S. L. Chin, Opt. Commun. **282**, 4283 (2009).
[34] T.-J. Wang, C. Marceau, Y. Chen, S. Yuan, F. Théberge, M. Châteauneuf, J. Dubois, and S. L. Chin, Appl. Phys. Lett. **96**, 211113 (2010).